Journal of Applied Physics

RESEARCH ARTICLE | APRIL 25 2022

Enhanced performance of supercapacitors based on rotationally stacked CVD graphene

W. Lisheshar Ibrahim; Hüseyin Şar; Feridun Ay; ... et. al

Journal of Applied Physics 131, 164302 (2022)
https://doi.org/10.1063/5.0084969

AIP Publishing

Journal of Applied Physics ARTICLE scitation.org/journal/jap

Enhanced performance of supercapacitors based on rotationally stacked CVD graphene

Cite as: J. Appl. Phys. **131**, 164302 (2022); doi: 10.1063/5.0084969
Submitted: 11 January 2022 · Accepted: 24 March 2022 ·
Published Online: 25 April 2022

W. Lisheshar Ibrahim,[1] Hüseyin Şar,[2] Feridun Ay,[1] and Nihan Kosku Perkgöz[1,a)]

AFFILIATIONS

[1]Department of Electrical and Electronic Engineering, Eskisehir Technical University, Eskisehir 26555, Turkey
[2]Interuniversity Microelectronic Center (IMEC), Leuven, Belgium

[a)]**Author to whom correspondence should be addressed:** nkperkgoz@eskisehir.edu.tr. **Tel.:** (0222) 321 35 50/6461

ABSTRACT

One of the main problems faced by 2D materials used in supercapacitor applications when scaling up is restacking, such that their gravimetric capacitances become dramatically inferior to that of their monolayer forms. This study analyzes the Raman spectra of transferred layers of CVD-graphene revealing decoupling and rotational stacking of layers, with the potential of retention of intrinsic monolayer properties. Rotationally stacked layers have the potential to mitigate restacking and, thus, are capable of easing ion intercalation and boosting their performance in supercapacitor applications. In this pursuit, binder-free supercapacitors are fabricated out of chemical vapor deposited bilayer graphene, successively transferred to form rotationally stacked multilayers. Supercapacitors constructed with rotationally stacked four-layer graphene have an incredible specific gravimetric capacitance of 316.1 F g^{-1} at 1 mV s^{-1}, with a corresponding energy density of 28.1 Wh kg^{-1} and ~100% capacitance retention at 10 000 cycles.

I. INTRODUCTION

Progress in technology has effected increasing energy consumption, which, in turn, has given birth to greenhouse gas emissions causing a considerable amount of research to be diverted toward sustainable and environment friendly sources of energy.[1,2] The intermittent nature of these energy sources has rendered them incapable of meeting up with ever-increasing energy demands, thus creating the need for energy storage systems such as lithium-ion batteries, supercapacitors, fuel cells, etc.[3–5] Despite having high power density, supercapacitors most often suffer from low energy storage capabilities.[6] The design of electrode materials with efficient charge storage capabilities is one of the multiple pathways taken to boost the capacity as well as the power density of supercapacitors. The discovery of 2D materials with extraordinary electrochemical properties has nonetheless fueled the drive to use them as supercapacitor electrode materials. However, supercapacitors based on 2D materials generally perform below expectations due to agglomeration problems incurred during material and or device processing.[7]

One of the most crucial factors in supercapacitor optimization and capacitance enhancement lies in materials micromachining, where trade-offs must inevitably be made between high power, energy density, and cycle stability.[8,9] Being cheap and earth-abundant, carbon is engineered for electrochemical double layer capacitor (EDLC) applications with high active surface area (3000 m^2 g^{-1} for activated carbon[10]) and good conductivity.[11] Activated carbon, carbide-derived-carbons, carbon nanotubes, carbon nanofibers, etc., have demonstrated capacitances up to 300 F g^{-1} and remarkable cycle stabilities (up to 10 000 charge–discharge cycles) in EDLC applications.[11] Pseudoactive materials, on the other hand, are capable of higher capacitance as seen in transition metal oxides such as MnO_2,[12,13] RuO_2,[14] transition metal sulfides, MnS,[15] conducting polymers,[16] and aerogels.[17] Unfortunately, these materials are usually less conductive and less cycle stable.[7] Progress in nanomaterial and nanotechnology is making it possible to design devices with improved performance, scalability, and compatibility with contemporary technology.[18] An intense research attention is being dedicated to developing nanomaterials with a high capacity for housing many electrolyte ions.[19] This has further been compounded with the discovery of two-dimensional materials opening doors for a myriad of new possible applications including sensing,[20,21] catalysis,[22,23] optoelectronics,[24] spintronics,[25–27] and energy storage,[28] just to mention a few. 2D materials being one or few atoms thick possess bare surface atoms,

which provide increased surface area.[7] For example, a single layer of graphene possesses an intrinsic specific capacitance of 21–28 μF cm^{-2} (about 551 F g^{-1} if all the area is utilized).[29,30] The edges of 2D materials contain dangling bonds making them more reactive. Some 2D materials such as MXenes also have wide van der Waals spacing that can easily intercalate electrolyte ions.[31] Despite having atomic thickness, 2D materials nonetheless have high mechanical strength (for example, graphene has a Young's modulus of ~1 TPa[32]), which is desirable in flexible energy storage devices. The research developments in 2D materials for supercapacitor applications are encapsulated by review articles such as those by Velasco *et al.*[33] and Kumar *et al.*[7]

2D materials can be synthesized via a myriad of methods. For example, graphene can be prepared by mechanical exfoliation, which is capable of producing the highest quality of graphene; however, it has neither high throughput nor high yield.[34] Other methods include PECVD, CVD,[35] chemical methods (e.g., liquid phase exfoliation), thermal decomposition of SiC, unzipping of CNT, etc.[36] Compared to other methods, CVD has a flush of merits such as repeatability, control of grain size, and layer number as well as mass production capabilities, as demonstrated by Bae *et al.*[37]

Even though there is much potential in 2D materials for application in energy storage, they often suffer from one drawback, which is the severe agglomeration occurring when they are synthesized into multiple layers, thus greatly limiting their gravimetric capacitances.[38] A handful of approaches have been suggested to mitigate this hurdle, such as the use of spacers,[39–41] *in situ* transformation,[42] fabrication of binder-free electrodes,[43,44] pre-electrolyte mediation,[45] etc. However, the resulting capacitances are still not comparable to those of their monolayer counterparts. Another attempt to overcome this obstacle involves hybridization of the electrode materials,[7] which, in addition to reducing agglomeration, produces a synergy in the electrochemical properties of the materials used. Functionalization of the active material with oxygen containing compounds have also been shown to improve the performance of carbon materials (e.g., graphene nanoribbons) by introducing pseudo-capacitance.[46] Ionic liquids as shown by Down and Banks[47] are conducive for high energy density supercapacitors due to their wide voltage window. This also requires materials to have large spore sizes due to macro-size ions.

Herein, Raman spectra analyses of rotationally stacked (RS) n-layer graphene—obtained by successive transfer of bilayer graphene—are carried out. These different layers of chemical vapor deposition grown (CVD-grown) graphene are then used as supercapacitor electrode materials, and their performance is explored with the aim to show that rotationally stacked graphene can help reduce restacking in multilayer graphene structures.

II. RESULTS AND DISCUSSION

A. Material characterization

Graphene was synthesized on Cu substrates by CVD according to Li *et al.*[48] with a few modifications (such as the ratio of CH_4 and H_2 gases, growth temperature, and duration) per our CVD system. The transfer of the as-grown graphene on Cu substrates onto the target substrates (Si/SiO_2 and Ti/Au) was done using two methods, i.e., photoresist assisted (PRA), and Poly(methyl methacrylate) (PMMA)/Poly(dimethylsiloxane) (PDMS) assisted (PPA) method reported by Suk *et al.*[49] Graphene samples obtained by the PRA method were observed to be continuous with negligible or no cracks as shown in Fig. 1(a) and Fig. S1(b) in the supplementary material. A drawback of this method is that it takes more time, i.e., about 12–24 h is required for the photoresist to solidify on the samples; nonetheless, the resist can easily dissolve in acetone. Another disadvantage is that the resist/graphene film is brittle and needs to be handled with extra care. In addition, the Raman spectra obtained from this sample [Fig. 1(b) and Fig. S1(b) in the supplementary material] had a wide and high intensity D band, which is telling of high defect density in the graphene sample. On the other hand, Raman spectra of graphene samples obtained by the PPA method [Fig. 1(c)] possessed a relatively small D band, indicating relatively lower defect density.[50] Still, PPA transferred samples were seen to have many cracks [Fig. S1(a) in the supplementary material]. This is due to the PMMA/PDMS film not readily adhering to the target substrate, necessitating the application of light pressure. The technique also requires the graphene to be grown on thicker Cu substrates as thinner Cu will twist upon spin coating with PMMA. Another issue with this method is the inability of PMMA to completely dissolve in hot acetone and could only be removed by annealing the sample at 350 °C for about 2 h.

Figures 1(b) and 1(c) shows the Raman spectra of graphene transferred onto 300 nm SiO_2 on Si substrates with the disorder-induced D peak identified at 1377 cm^{-1}, a G band at 1597 cm^{-1}, a D$^{\#}$ at 2453 cm^{-1}, and a 2D (G′) Raman mode at 2681 cm^{-1} (measured with a 532 nm laser at 1 mW power), all in close agreement with the literature.[51] The 2D/G peak intensity ratio (2D/G PIR) is calculated as 1.31 and 1.01 for the PRA and PPA graphene, respectively. These values being between 1 and 2 and with the 2D band FWHM of 46.1 cm^{-1} indicate bilayer graphene.

The AFM topographic image of the PRA transferred sample is shown in Fig. 1(d). The thickness of the samples measured from the line profiles drawn on the AFM images varied from 1.8 nm [Figs. S1 (c) and S1(d) in the supplementary material] to 6 nm with an average thickness of 3.2 nm as shown in Fig. 1(e). This deviates from what is reported in the literature (i.e., 0.335 nm for monolayer and 0.81 nm for bilayer graphene).[52,53] The 3D AFM image of the graphene is shown in Fig. 1(f) with an average roughness of 1.8 nm, which accounts for the increase in measured thickness. Studies have also shown that AFM is not very reliable for determining the thickness of graphene, especially for single-layer graphene with reported values ranging from 0.4 to 1.7 nm, which differs markedly from the interlayer separation of graphite (0.335 nm) reported in the literature. This is especially true for CVD-grown graphene due to air bubbles or water molecules that get trapped between the graphene and the substrate during transfer, making it difficult to measure the correct thickness.[53]

The Raman spectra of different layers of graphene, stacked together by repeated PRA transfer (chosen due to successful transfer with no cracks), are illustrated in Fig. 2(a). Both the G and the 2D bands were observed to undergo blue shifts [Fig. 2(a) and Table I] as the number of layers increased. The 2D/G PIR increased with the number of layers, as shown in Table I. This is contrary to previously reported literature results, where the Raman 2D/G PIR of multiple layer graphene fell as the number of layers waxed.[54,55] The 2D band underwent an upshift, explaining the increase in the

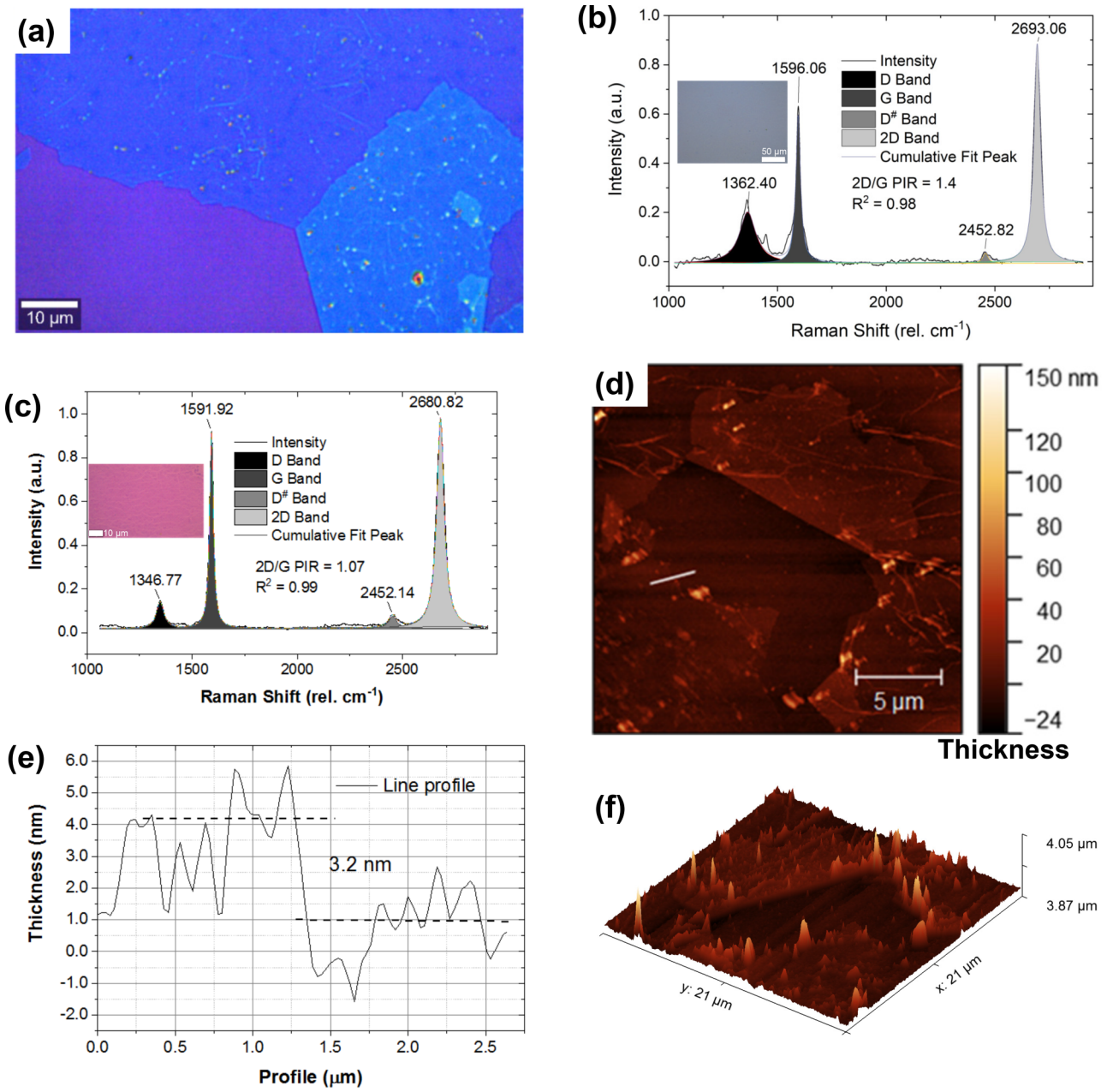

FIG. 1. (a) Optical microscopic image of PRA graphene taken from the edge of the sample. (b) The Raman spectra of PRA graphene. Inset: Optical image of PRA graphene, taken from the middle of the sample. (c) Raman spectra of PPA graphene. Inset: Optical image PPA graphene. (d) AFM image of the graphene sample transferred onto Si/SiO_2 by PRA method. (e) Line profile of graphene showing measured thickness. (f) 3D AFM image of PRA graphene.

2D/G PIR with the increase in the number of layers. This upshift in the 2D band is an indication of separation (decoupling) according to previous studies.[49,56] After intensity normalization and baseline subtraction [Fig. 2(a) inset], the Raman spectra of the stacked layers of graphene are almost identical, indicating that the increase in the 2D/G PIR is largely due to suspension. This increase in 2D/G PIR of the decoupled layers of graphene is a consequence of the etalon effect in the 300 nm SiO_2 cavity and decrease in doping due to the decoupling of graphene from the substrate or the lower layer.[49] This only explains the upshift in the 2D mode; however, the fact that the

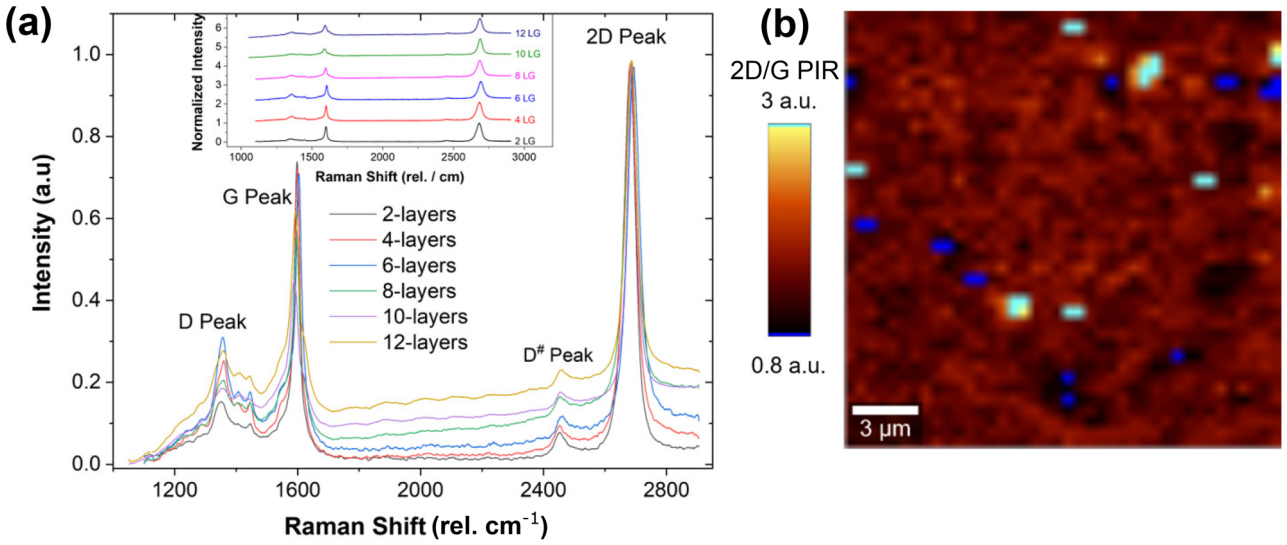

FIG. 2. Raman analysis of stacked layers of graphene. (a) Average Raman spectra of 2- to 12-layer graphene. Inset: Intensity normalized Raman spectra of the stacked graphene. (b) 2D/G PIR spatial map of six-layer graphene.

Raman spectra of the layer were identical [Fig. 2(a) inset] after baseline correction can be explained by considering the crystallographic stacking of graphene. Two orders of crystallographic stacking, AB and ABC, are observed in graphite and have been shown to strongly influence its electronic[57–59] and vibrational[42,60,61] properties. A third stacking order, rotational or the moiré pattern, is observed when two graphene layers are placed on top of each other.[57,61] Studies on the Raman spectra of graphene and misoriented graphene show that weak interaction between the twisted graphene layers alter the phonon dispersion curve relative to graphene, while leaving the electronic band structure typically untouched.[59] These studies suggest the preservation of the intrinsic electronic properties of graphene in twisted few-layer graphene with a rotational angle larger than 20°.[58]

Raman spatial maps from three different samples were examined to understand how this decoupling occurred among the graphene layers. For this reason, the 2D/G PIR was then filtered from the spatial maps as shown in Fig. 2(b) for six layers of graphene. Similarly, the same procedure is applied to two layers and four layers of graphene to confirm the same effect as shown in Fig. S2 in the supplementary material. Apart from the increase in the 2D/G PIR value with number of layers, there is no significant difference between the three images. The areas with the lowest 2D/G PIR are shaded in blue and correspond to multilayered regions of the sample. These can be viewed as the regions where the graphene layers interact with one another, which explains the structure of the suspension of graphene layers. Our suggestion is supported by the 3D AFM topographic results of bilayer graphene, which is shown in Fig. 1(f) where nanopillars were formed presumably due the photoresist residues. These nanopillars can be regarded as the points where the bottom layers are hinged to the top layers, leaving the area in between them suspended or decoupled. This means that agglomeration of graphene layers will be markedly reduced if these graphene samples are used as the electrode material for supercapacitors, with the potential of easing ion intercalation and as such boosting their charge storage capability.

TABLE I. Raman modes for different layers of stacked graphene.

Number of layers	Position of Raman mode				2D/G PIR
	D mode	G mode	D# mode	2D mode	
2	1377.0	1597.8	2454.7	2680.5	1.31
4	1370.6	1598.9	2457.6	2682.5	1.36
6	1374.3	1603.3	2461.5	2693.1	1.40
8	1380.5	1595.4	2456.5	2685.3	1.88
10	1388.5	1588.3	2458.5	2688.4	2.56
12	1374.7	1592.3	2462.3	2686.1	1.76

B. Supercapacitor application

The CVD-grown graphene samples were transferred two layers at a time to obtain multiple layers of rotationally stacked graphene (RS-graphene), which were then used to fabricate supercapacitors. Their performance was evaluated via cyclic voltammetry (CV), electrochemical impedance spectroscopy (EIS), and constant current charge–discharge (CCCD) (Fig. 3). To determine the rate stability of the supercapacitors, CV was performed at different scan rates. Figures 3(a)–3(c) illustrate the CV of supercapacitors based on two-, four-, and eight-layer RS-graphene at varied scan rates. As seen from the CVGs, the fabricated devices exhibited electrochemical double layer capacitor (EDLC) behavior, with negligible or no

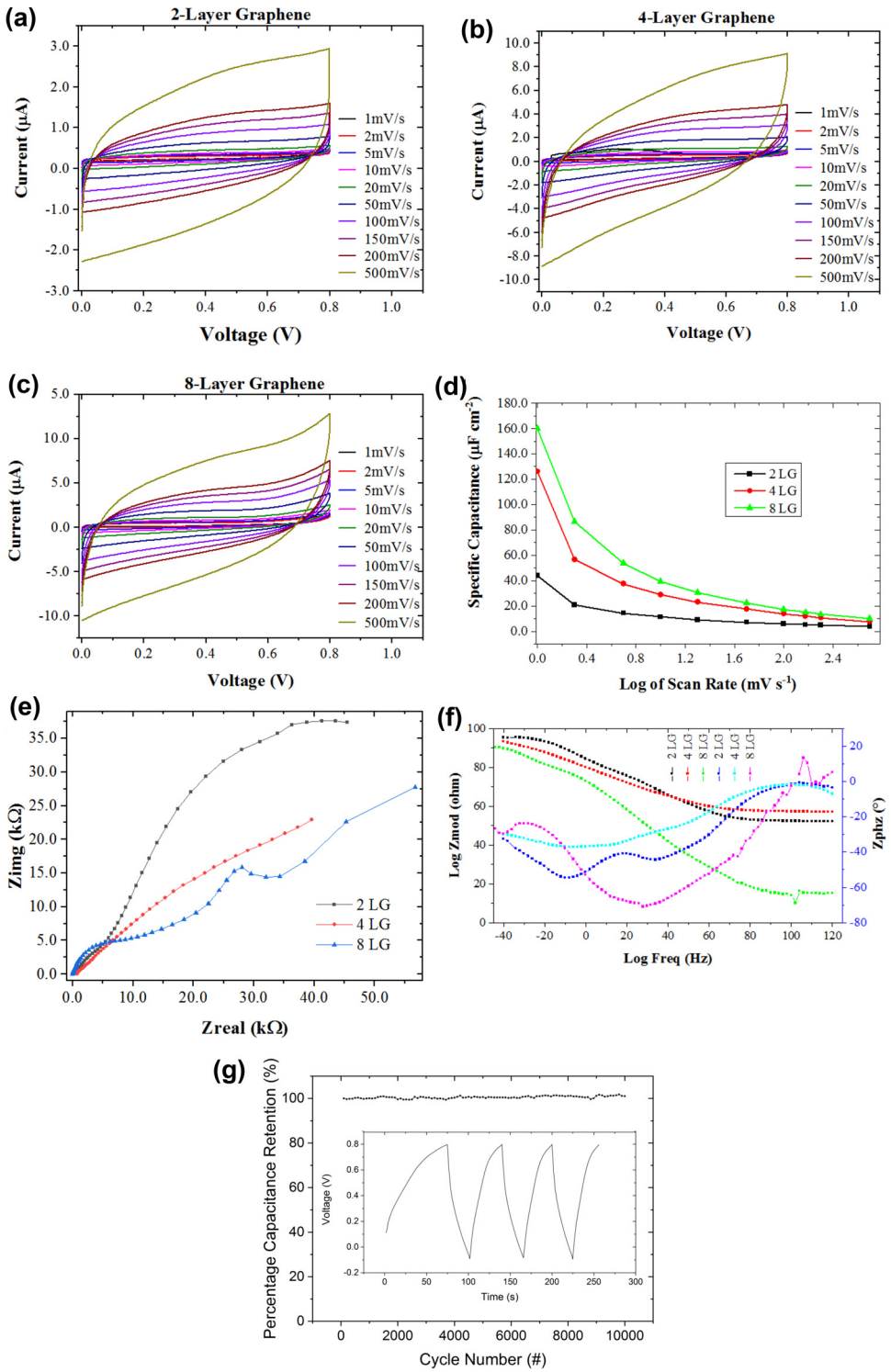

FIG. 3. Electrochemical characterization of graphene supercapacitors: (a) Cyclic voltammograms (CVGs) of monolayer graphene at different scan rates; (b) CVGs of bilayer graphene supercapacitor; (c) CVGs of supercapacitor with 4-layer graphene as active material. (d) Nyquist plot of the supercapacitor; (e) frequency response (Bode plot) of the four-layer RS-graphene supercapacitor; (f) CCCD response of the supercapacitor constructed with four-layer RS-graphene.

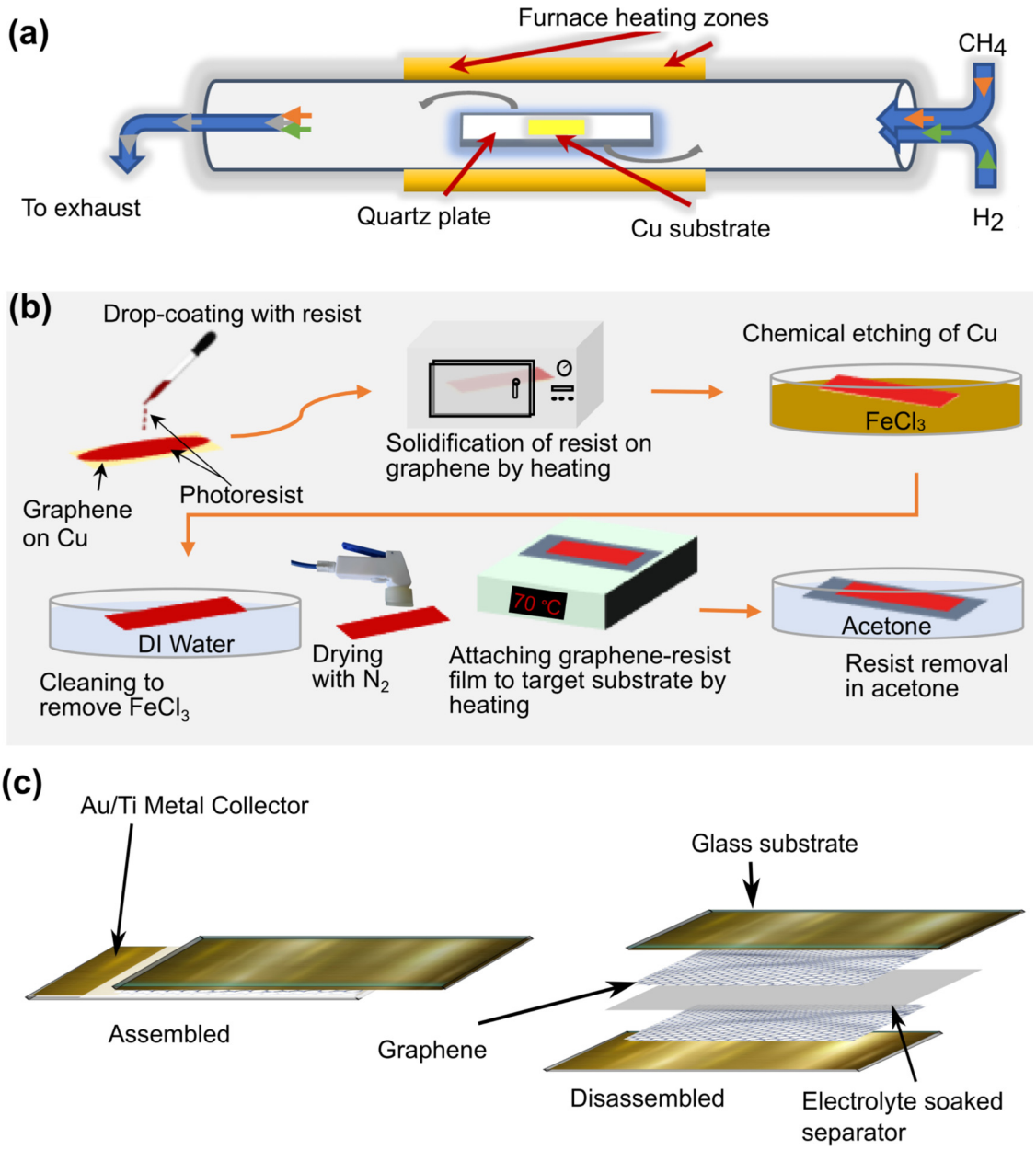

FIG. 4. (a) CVD growth setup for graphene. (b) Flow diagram of the PRA transfer method. (c) Supercapacitor device architecture before and after assembling.

pseudocapacitive effect, evident from the rectangular nature of their CVGs, which is maintained even at high scan rates. This also proves that there is no contribution from resist residues to the calculated capacitance since photoresist is a non-conductive polymer and will only possibly contribute pseudo-actively. Capacitances of a single electrode at different scan rates were calculated from the area enclosed by the CV using Eq. (S1) in the supplementary material, similar to previous studies.[62,63] The bilayer graphene supercapacitor was measured with a specific capacitance of 43.9 μF cm^{-2}, corresponding to a gravimetric capacitance of 239.3 F g^{-1} (volumetric capacitance of 542.4 F cm^{-3}) at a scan rate of 1 mV s^{-1}.

Figure 3(d) illustrates the variation of specific capacitance with the logarithm of the scan rate—for better visibility—for different active material thicknesses (two, four, and eight layers), which increased from 43.9 to 160.2 μF cm^{-2}. The gravimetric capacitance decreased with the scan rate, i.e., from 239.3 F g^{-1} at

1 mV s^{-1} to 21.4 F g^{-1} at 500 mV s^{-1} with a rate capability of only 8.9%. The highest gravimetric capacitance, 316.1 F g^{-1} at 1 mV s^{-1} and 141.8 F g^{-1} at 2 mV s^{-1}, was obtained from four layers of RS-graphene. A possible reason for increase in capacitance of four-layer RS-graphene relative to two-layer RS-graphene is due to no-restacking and the availability of three intercalation sites instead of only one in the two-layer graphene. Eight layers of RS-graphene demonstrated a rather inferior capacitance of 193.0 and 104.6 F g^{-1} at scan rates of 1 and 2 mV s^{-1}, respectively. Specific energy densities of 16.3, 28.1, and 16.8 Wh kg^{-1} were calculated for two, four, and eight layers of RS-graphene, respectively.

Figure 3(e) shows the impedance response of the two, four, and six-layer graphene supercapacitors, which can be used to estimate the equivalent series resistance (ESR) as explained in previous studies.[64,65] The internal resistance[66,67] (i.e., the sum of the bulk electrolyte resistance and the charge transfer resistance) values for two-, four-, and eight-layer RS-graphene were calculated as 427.2, 697.5, and 685.8 Ω, respectively. The values of the ESR could not be extracted due to frequency limitations of our device. The bode plot [Fig. 3(f)] illustrates the phase angle approaching zero at high frequencies, indicating the influence of the ESR. Figure 3(g) shows the percentage capacitance retention of the four-layer RS-graphene supercapacitor obtained after 10 000 charge–discharge cycles (plotted as the average after every 100 points for better visualization). The charge capacity remains constant after 10 000 cycles indicating a 100% charge retention capability at a current density of 10 A g^{-1}.

Compared with previously reported graphene supercapacitors, RS-graphene supercapacitors have superior gravimetric capacitance at a scan rate of 1 mV s^{-1} (Table S1 in the supplementary material). As mentioned above, such excellent electrochemical performance is attributed to increased electrolyte ion intercalation.

III. CONCLUSION

A continuous film of bilayer graphene synthesized by CVD is transferred repeatedly using the PRA method to form multiple layers of RS-graphene. μRaman spectral analyses of the samples revealed that the layers were suspended from each other unlike in the *in situ* grown multilayer graphene. Repeated transfer of graphene can greatly reduce the problem of agglomeration faced by bulk graphene (graphite) and other two-dimensional materials, making it possible for the effective intercalation of electrolytes ions. This was supported by the incredible performance of four-layer RS-graphene reaching 316 F g^{-1}, which is remarkable for carbon-based materials. One of the problems faced while working with graphene is that it loses its intrinsic properties as the number of layers increases. Repeated transfer suggests that these intrinsic properties could be preserved even in multilayer RS-graphene, which can be exploited for many other applications in optoelectronics, sensing, and so forth.

IV. EXPERIMENTAL SECTION

The electrode materials were grown as described by Li *et al.*[48] in a custom-made CVD system using a setup illustrated in Fig. 4(a). To grow the graphene, the Cu substrates were first cleaned in acetone, IPA, and de-ionized (DI) water and dried with N_2. The experimental setup was as shown in Fig. 4(a), in which the reactor was heated to 1035 °C under the flow of H_2, after which CH_4 was then introduced for the duration of the experiment, and the furnace was allowed to cool down naturally.

The samples grown on Cu substrates were transferred to target substrates (Au/Ti) using a photoresist assisted transfer technique shown in Fig. 4(b). First, these samples were cut into desired pieces, drop coated with a photoresist, and baked in a drying oven at 70 °C for a minimum of 12 h to allow the resist to solidify. Afterward, the Cu substrate was etched away using a 1M $FeCl_3$ solution, and a graphene-resist film remained afloat the solution. This was then removed, cleaned in DI water, dried with N_2, and placed onto the target substrates (SiO_2 or Au/Ti). The new substrate with the resist film was baked on a hotplate at 70 °C for 15 min to enable the resist/graphene film to stick, then removed, and finally the photoresist was dissolved in a bath of acetone.

Figure 4(c) shows the schematics of the supercapacitors used in this study. This was fabricated on cleaned glass substrates by first coating the substrates with 10 nm Ti, followed by 90 nm of Au, which served as the current collectors. The active material (graphene) was then transferred onto the Au/Ti current collectors, leaving the contacts uncovered. Finally, the electrolyte (1 M Na_2SO_4) soaked separator was placed between two electrodes and arranged as shown in the figure. The devices were encapsulated with Polyethylene terephthalate (PET) to avoid evaporation of the electrolyte during testing which was done using a Gamry Potentiostat.

The optical images were taken using Nikon Eclipse LV100NDA optical microscope while the Raman characterization of the samples was done using the WITec alpha-300R Raman system. The AFM results were obtained using NonoMagnetics-ezAFM™.

SUPPLEMENTARY MATERIAL

The supplementary material contains additional information on the transferred samples, AFM results, Raman spatial map of two- and four-layer graphene, and comparison of the performance of our supercapacitor with the state of the art.

ACKNOWLEDGMENTS

This work was supported by TÜBİTAK—The Scientific and Technological Research Council of Turkey under Project Nos. 118E996 and 20AG025 and under Program No. TÜBİTAK 20AG001. The authors greatly appreciate the use of equipment from the Material Engineering Laboratory of Eskişehir Technical University, under Professor Dr. Servet TURAN.

NOMENCLATURE

AFM	Atomic force microscopy
CCCD	Constant current charge discharge
CV	Cyclic voltammetry
CVD	Chemical vapor deposition
EDLC	Electrochemical double layer capacitor
EIS	Electrochemical impedance spectroscopy
ESR	Equivalent series resistance
PIR	Peak intensity ratio

PPA	PMMA/PDMS assisted
PPA and PRA graphene	Graphene transferred using PPA and PRA methods, respectively
PRA	Photoresist assisted

AUTHOR DECLARATIONS

Conflict of Interest

The authors have no conflicts to disclose.

DATA AVAILABILITY

The authors confirm that the data available to support the findings of this study are found within the article and its supplementary material. Raw data supporting the findings of this work are available from the corresponding author upon reasonable request.

REFERENCES

[1]Z. Yu, B. Duong, D. Abbitt, and J. Thomas, Adv. Mater. **25**, 3302 (2013).
[2]Z. Yu, C. Li, D. Abbitt, and J. Thomas, J. Mater. Chem. A **2**, 10923 (2014).
[3]V. Etacheri, R. Marom, R. Elazari, G. Salitra, and D. Aurbach, Energy Environ. Sci. **4**, 3243 (2011).
[4]A. Mohapatra and S. Tripathy, IOP Conf. Ser. Mater. Sci. Eng. **377**, 012135 (2018).
[5]Z. Yu, L. Tetard, L. Zhai, and J. Thomas, Energy Environ. Sci. **8**, 702 (2015).
[6]B. E. Conway, *Electrochemical Supercapacitors: Scientific Fundamentals and Technological Applications* (Springer Science & Business Media, 2013).
[7]K. S. Kumar, N. Choudhary, Y. Jung, and J. Thomas, ACS Energy Lett. **3**, 482 (2018).
[8]A. Burke, J. Power Sources **91**, 37 (2000).
[9]M. Vangari, T. Pryor, and L. Jiang, J. Energy Eng. **139**, 72 (2013).
[10]P. Simon and A. Burke, Electrochem. Soc. Interface **17**, 38 (2008).
[11]R. Dubey and V. Guruviah, Ionics **25**, 1419 (2019).
[12]M. Huang, F. Li, F. Dong, Y. X. Zhang, and L. L. Zhang, J. Mater. Chem. A **3**, 21380 (2015).
[13]G. Yu, L. Hu, N. Liu, H. Wang, M. Vosgueritchian, Y. Yang, Y. Cui, and Z. Bao, Nano Lett. **11**, 4438 (2011).
[14]Y.-T. Kim, K. Tadai, and T. Mitani, J. Mater. Chem. **15**, 4914 (2005).
[15]R. B. Pujari, A. C. Lokhande, A. A. Yadav, J. H. Kim, and C. D. Lokhande, Mater. Des. **108**, 510 (2016).
[16]M. A. A. Mohd Abdah, N. H. N. Azman, S. Kulandaivalu, and Y. Sulaiman, Mater. Des. **186**, 108199 (2020).
[17]Q. Yang, J. Yang, Z. Gao, B. Li, and C. Xiong, ACS Appl. Energy Mater. **3**, 1145 (2020).
[18]E. Martínez-Periñán, M. P. Down, C. Gibaja, E. Lorenzo, F. Zamora, and C. E. Banks, Adv. Energy Mater. **8**, 1702606 (2018).
[19]T. Palaniselvam and J.-B. Baek, 2D Mater. **2**, 032002 (2015).
[20]P. Bollella, G. Fusco, C. Tortolini, G. Sanzò, G. Favero, L. Gorton, and R. Antiochia, Biosens. Bioelectron. **89**, 152 (2017).
[21]S. Feng, Z. Lin, X. Gan, R. Lv, and M. Terrones, Nanoscale Horiz. **2**, 72 (2017).
[22]D. Deng, K. S. Novoselov, Q. Fu, N. Zheng, Z. Tian, and X. Bao, Nat. Nanotechnol. **11**, 218 (2016).
[23]A. Hasani, M. Tekalgne, Q. V. Le, H. W. Jang, and S. Y. Kim, J. Mater. Chem. A **7**, 430 (2019).
[24]J. Cheng, C. Wang, X. Zou, and L. Liao, Adv. Opt. Mater. **7**, 1800441 (2019).
[25]I. Choudhuri, P. Bhauriyal, and B. Pathak, Chem. Mater. **31**, 8260 (2019).
[26]W. Liu and Y. Xu, *Spintronic 2D Materials: Fundamentals and Applications* (Woodhead Publishing, 2019).
[27]S. Wei, X. Tang, X. Liao, Y. Ge, H. Jin, W. Chen, H. Zhang, and Y. Wei, Mater. Res. Express **6**, 122004 (2019).
[28]X. Zhang, L. Hou, A. Ciesielski, and P. Samorì, Adv. Energy Mater. **6**, 1600671 (2016).
[29]M. D. Stoller, C. W. Magnuson, Y. Zhu, S. Murali, J. W. Suk, R. Piner, and R. S. Ruoff, Energy Environ. Sci. **4**, 4685 (2011).
[30]J. Xia, F. Chen, J. Li, and N. Tao, Nat. Nanotechnol. **4**, 505 (2009).
[31]B.-M. Jun, S. Kim, J. Heo, C. M. Park, N. Her, M. Jang, Y. Huang, J. Han, and Y. Yoon, Nano Res. **12**, 471 (2019).
[32]C. Lee, X. Wei, J. W. Kysar, and J. Hone, Science **321**, 385 (2008).
[33]A. Velasco, Y. K. Ryu, A. Boscá, A. Ladrón-de-Guevara, E. Hunt, J. Zuo, J. Pedrós, F. Calle, and J. Martinez, Sustainable Energy Fuels **5**, 1235 (2021).
[34]C. N. R. Rao, A. K. Sood, K. S. Subrahmanyam, and A. Govindaraj, Angew. Chem. Int. Ed. **48**, 7752 (2009).
[35]C. Mattevi, H. Kim, and M. Chhowalla, J. Mater. Chem. **21**, 3324 (2011).
[36]W. Choi, I. Lahiri, R. Seelaboyina, and Y. S. Kang, Crit. Rev. Solid State Mater. Sci. **35**, 52 (2010).
[37]S. Bae, H. Kim, Y. Lee, X. Xu, J.-S. Park, Y. Zheng, J. Balakrishnan, T. Lei, H. Ri Kim, Y. I. Song, Y.-J. Kim, K. S. Kim, B. Özyilmaz, J.-H. Ahn, B. H. Hong, and S. Iijima, Nat. Nanotechnol. **5**, 574 (2010).
[38]Q. Ke and J. Wang, J. Materiomics **2**, 37 (2016).
[39]L. Qiu, X. Yang, X. Gou, W. Yang, Z.-F. Ma, G. G. Wallace, and D. Li, Chem. Eur. J. **16**, 10653 (2010).
[40]Y. Si and E. T. Samulski, Chem. Mater. **20**, 6792 (2008).
[41]G. Wang, X. Sun, F. Lu, H. Sun, M. Yu, W. Jiang, C. Liu, and J. Lian, Small **8**, 452 (2012).
[42]M. Guo, J. Wang, H. Dou, G. Gao, S. Wang, J. Wang, Z. Xiao, G. Wu, X. Yang, and Z.-F. Ma, Nano Energy **56**, 502 (2019).
[43]R. K. Mishra, M. Krishnaih, S. Y. Kim, A. K. Kushwaha, and S. H. Jin, Mater. Lett. **236**, 167 (2019).
[44]R. A. Perera Jayawickramage, K. J. Balkus, and J. P. Ferraris, Nanotechnology **30**, 355402 (2019).
[45]N. He, S. Patil, J. Qu, J. Liao, F. Zhao, and W. Gao, ACS Appl. Energy Mater. **3**, 2949 (2020).
[46]M. Qorbani, A. Esfandiar, H. Mehdipour, M. Chaigneau, A. Irajizad, and A. Z. Moshfegh, ACS Appl. Energy Mater. **2**, 3665 (2019).
[47]M. P. Down and C. E. Banks, ACS Appl. Energy Mater. **1**, 891 (2018).
[48]X. Li, W. Cai, J. An, S. Kim, J. Nah, D. Yang, R. Piner, A. Velamakanni, I. Jung, E. Tutuc, S. K. Banerjee, L. Colombo, and R. S. Ruoff, Science **324**, 1312 (2009).
[49]J. W. Suk, A. Kitt, C. W. Magnuson, Y. Hao, S. Ahmed, J. An, A. K. Swan, B. B. Goldberg, and R. S. Ruoff, ACS Nano **5**, 6916 (2011).
[50]A. Eckmann, A. Felten, A. Mishchenko, L. Britnell, R. Krupke, K. S. Novoselov, and C. Casiraghi, Nano Lett. **12**, 3925 (2012).
[51]L. M. Malard, M. A. Pimenta, G. Dresselhaus, and M. S. Dresselhaus, Phys. Rep. **473**, 51 (2009).
[52]K. S. Novoselov, D. Jiang, F. Schedin, T. J. Booth, V. V. Khotkevich, S. V. Morozov, and A. K. Geim, Proc. Natl. Acad. Sci. U.S.A. **102**, 10451 (2005).
[53]H. Shioyama, Synth. Met. **114**, 1 (2000).
[54]A. C. Ferrari, J. C. Meyer, V. Scardaci, C. Casiraghi, M. Lazzeri, F. Mauri, S. Piscanec, D. Jiang, K. S. Novoselov, S. Roth, and A. K. Geim, Phys. Rev. Lett. **97**, 187401 (2006).
[55]A. Gupta, G. Chen, P. Joshi, S. Tadigadapa, and Eklund, Nano Lett. **6**, 2667 (2006).
[56]A. A. Balandin, S. Ghosh, W. Bao, I. Calizo, D. Teweldebrhan, F. Miao, and C. N. Lau, Nano Lett. **8**, 902 (2008).
[57]K. F. Mak, J. Shan, and T. F. Heinz, Phys. Rev. Lett. **104**, 176404 (2010).
[58]A. Lucian, G. Li, A. Reina, J. Kong, R. R. Nair, K. S. Novoselov, A. K. Geim, and E. Y. Andrei, Phys. Rev. Lett. **106**, 126802 (2011).
[59]P. Poncharal, A. Ayari, T. Michel, and J. L. Sauvajol, Phys. Rev. B **78**, 113407 (2008).
[60]C. H. Lui, Z. Li, Z. Chen, P. V. Klimov, L. E. Brus, and T. F. Heinz, Nano Lett. **11**, 164 (2011).

[61]V. Carozo, C. M. Almeida, E. H. M. Ferreira, L. G. Cançado, C. A. Achete, and A. Jorio, Nano Lett. **11**, 4527 (2011).
[62]A. Allagui, T. J. Freeborn, A. S. Elwakil, and B. J. Maundy, Sci. Rep. **6**, 38568 (2016).
[63]M. D. Stoller and R. S. Ruoff, Energy Environ. Sci. **3**, 1294 (2010).
[64]F. Lufrano, P. Staiti, and M. Minutoli, J. Power Sources **124**, 314 (2003).
[65]B.-A. Mei, O. Munteshari, J. Lau, B. Dunn, and L. Pilon, J. Phys. Chem. C **122**, 194 (2018).
[66]C. Lei, F. Markoulidis, Z. Ashitaka, and C. Lekakou, Electrochim. Acta **92**, 183 (2013).
[67]I. Yang, S.-G. Kim, S. H. Kwon, M.-S. Kim, and J. C. Jung, Electrochim. Acta **223**, 21 (2017).